H. Lannay, S. Fouvry, B. Berthel, C. Gandiolle, J. Neggers, G. Paramucchio, Stability of the critical distance method for fretting cracking prediction: influence of microstructure and crack nucleation size, TI 186 (2023) 108570

(https://doi.org/10.1016/j.triboint.2023.108570).

Stability of the critical distance method for fretting cracking prediction: influence of microstructure and crack nucleation size

Hugo Lannay[a,*], Siegfried Fouvry[a,*], Bruno Berthel[a], Camille Gandiolle[b,*], Jan Neggers[b], Gabriel Paramucchio[a]

[a]: *LTDS – Laboratoire de Tribologie et Dynamique des Systèmes, Ecole Centrale de Lyon, 36 avenue Guy de Collongue, 69134 Ecully, France*

[b]: *Université Paris-Saclay, CentraleSupélec, ENS Paris-Saclay, CNRS, LMPS – Laboratoire de Mécanique Paris-Saclay, 91190 Gif-sur-Yvette, France*

* C*orresponding authors*: hugo.lannay@ec-lyon.fr (H. Lannay), siegfried.fouvry@ec-lyon.fr (S. Fouvry), camille.gandiolle@centralesupelec.fr (C. Gandiolle)

ABSTRACT

To provide lifetime predictions of metal pieces under fretting-fatigue loading, the crack initiation process has to be understood. However, there is no consensus in the literature over the crack nucleation length. The objective of this study is to understand the link between fretting crack nucleation and microstructure to resolve this question of the critical crack nucleation size. For this purpose, cylinder/plane fretting tests were performed to plot the evolution of the crack length as a function of tangential load amplitude. Finally, a link between the critical distance, evaluated by inverse method, and the grain size is established for different crack nucleation lengths. The investigation suggests that the critical distance evolution depends on the considered defect size.

Keywords: fretting, fatigue, defects, finite-element method

Highlights:

- Influence of the grain size on the fatigue and fretting properties
- Obtaining crack arrest properties obtained by FEM simulations
- Dependence of the critical distance on the crack nucleation length

Nomenclature

a: half-width of the cylinder/plane contact (mm)
b: projected crack length (µm)
b_0: short cracks / long cracks transition (µm)
b_{CN}: crack nucleation length (µm)
d: grain size (µm)
E: Young's modulus (GPa)
E%: mean relative error between the calculated critical distance and the fitted value
f: frequency (Hz)
HV: Vickers hardness
K_I: stress intensity factor mode I (MPa√m)
K_{II}: stress intensity factor mode II (MPa√m)
ℓ_d: critical distance (µm)
N: number of cycles
N_{max}: maximum number of cycles in fatigue tests
p: Hertz contact pressure (MPa)
P: linear normal load (N/mm)
Q: linear tangential load (N/mm)
Q*: linear tangential load amplitude (N/mm)
Q^*_0: linear tangential load where the fretting fitted curve crosses the horizontal axis (N/mm)
Q^*_{CN}: crack nucleation linear tangential load amplitude (N/mm)
R: fatigue ratio
x: position from the centre of the cylinder/plane contact in the sliding direction (mm)
z: depth under the contact (mm)
α_b: slope of fretting fitting curves (µm.mm/N)
Γ_{SWT}: SWT criterion parameter (MPa)
δ: fretting displacement (µm)
δ*: fretting displacement amplitude (µm)
ΔK: stress intensity factor range (MPa√m)
ΔK_0: stress intensity factor range threshold related to the long crack arrest condition (MPa√m)
ΔK_{th}: stress intensity factor range threshold related to crack arrest condition (MPa√m)
ε: strain
σ: stress (MPa)
$\sigma_{d,-1}$: traction-compression fatigue limit with a -1 ratio (MPa)
σ_{eq}: criterion equivalent stress (MPa)
σ_{max}: maximum stress in a fatigue test (MPa)
σ_{SWT}: SWT criterion equivalent stress (MPa)
σ_u: ultimate tensile strength (MPa)
σ_y: yield strength (MPa)
ν: Poisson coefficient
ψ_{l_d}: ℓ_d/b_0 ratio
$\psi_{l_d,SG}$: ℓ_d/b_0 constant ratio for small grain sizes
$\psi_{l_d,LG}$: ℓ_d/b_0 constant ratio for large grain sizes

1. Introduction

In metallic assemblies, fretting can be the source of severe damage. When in partial slip regime, it causes crack nucleation that can lead to the complete failure of the material [1,2]. To avoid that problem, several multiaxial fatigue criteria exist to predict the crack risk [3–5]. Usually, these criteria are applied at the hotspot, where the stress is the highest.

However, in the case of high-stress gradients, such as in plain fretting or fretting-fatigue for example, these criteria over-estimate the crack nucleation risk [6,7], which means they predict cracks in cases where none exists, which leads to significant over-dimensioning in industrial applications.

One way to overcome this issue is to use a non-local approach such as the critical distance method described by Taylor [8,9] in his Theory of Critical Distances. Instead of using fatigue criteria at the hotspot as usual, they are calculated at a certain distance below the hotspot called the critical distance ℓ_d (Figure 1). This specific non-local approach is called Point Method as the stress state is analysed only at one specific point under the hotspot.

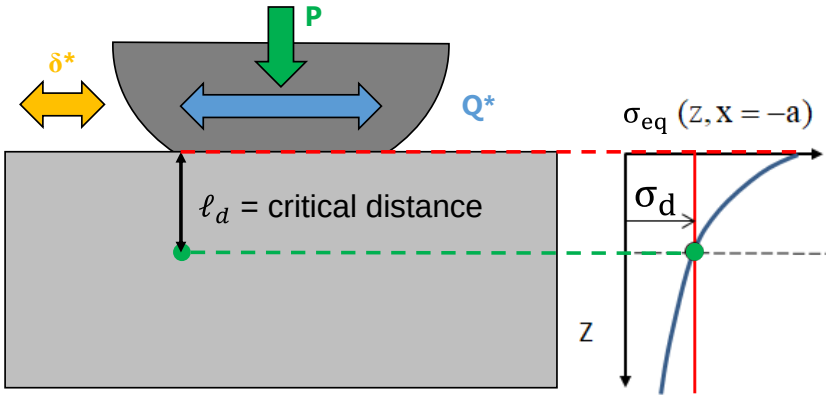

Figure 1: Definition of the critical distance.

Non-local approaches can also be applied to wider areas. It is possible to consider the stress along a line under the hotspot (Line Method) or inside a volume around the hotspot (Volume Method) or a process volume approach [7,10].

The critical distance method provides better crack nucleation predictions, as demonstrated by Ferré *et al.* [6], and many papers use it for simplicity and accuracy. In the literature, two main ways of determining the critical distance can be found. The first one is an inverse calibration method. It consists in taking the distance to the hotspot at which the multiaxial fatigue criterion is validated for specific conditions (microstructure, geometries, loadings, …). Then this critical distance is applied to all other conditions to determine crack nucleation risk (examples in [11–15]). In this case, an arbitrary length is usually chosen as the crack nucleation length (10µm, 20µm, 50µm, …) to determine the crack nucleation tangential load threshold and then estimate the critical distance. The main advantage of this method is that it only needs a few experimental fretting tests to determine the critical distance parameter, and then all other crack nucleation conditions can be predicted numerically. However, there is no consensus in the literature over which length has to be chosen as the crack nucleation length, and this method does not take into account the effect of the microstructure or the stress gradient.

The second method to determine the critical distance consists in applying Taylor's approximation [16]. Indeed, Taylor defines the critical distance as $b_0/2$ with b_0 the short/long crack transition on the Kitagawa-Takahashi diagram [17]. This approximation is obtained for the application of the internal crack model of Westergaard [18]. Lots of papers [19–22] directly apply this approximation to determine the critical distance, using the b_0 given by the El Haddad parameter [23,24]. This method is interesting as there is no need for fretting tests to determine the critical distance. Yet, the fatigue limit and the stress intensity factor threshold have to be known to calculate the El Haddad parameter, which means fatigue and CT test campaigns for each material. Moreover, there is currently no physical explanation of why Taylor's approximation works and this approximation is linked to no specific crack nucleation length.

The objective of this study is to understand the link between fretting crack nucleation and microstructure, to resolve the question of the critical crack nucleation size. As fretting crack nucleation depends on the critical distance, this study aims to establish a physical description of the critical distance relative to the microstructure. Indeed, several papers have shown that the grain size influences the fatigue limit [25–28] and the fretting crack nucleation [29]. More specifically, the finer microstructures were shown to have a higher fatigue limit than coarser ones. To investigate the influence of the microstructure on the fretting crack nucleation, heat treatments were performed on a medium-carbon steel to obtain a wide range of grain sizes for the same material. This is important to note that, by changing the grain size, the material strength is inevitably modified too, and so the effect of the microstructure is correlated to the effect of mechanical properties. This is why fatigue analyses were performed for each heat-treated material to separate the microstructure effect over the stability of the critical distance method. As a consequence, the fluctuation of the mechanical properties associated with each microstructure was taken into account in the simulations and the evolution of the stability of the critical distance is considered to be decorrelated to this fluctuation. This lets us suppose that this analysis makes it possible to decouple the effect of the microstructure (i.e. grain size) regarding the stability of the critical distance method.

In addition, to discuss the nucleation question, three crack nucleation length scales will be considered: b_{CN}= 0µm (which is the theoretical crack nucleation), b_{CN}= d (diameter of the grain size) and b_{CN}= b_0 (short/long cracks transition). Considering the Kitagawa-Takahashi description of the evolution of the crack arrest stress intensity factor threshold ΔK_{th} versus the crack length b, it is interesting to note a difference in the evolution at b= b_0 (Figure 2). Therefore, the length scale b_0 appears like the grain size d as an interesting crack nucleation flow to calibrate the fretting crack process.

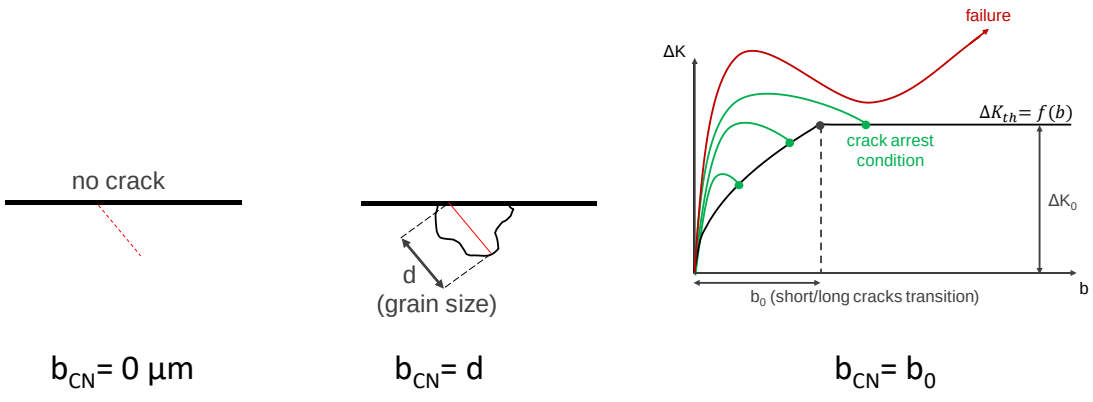

Figure 2: Illustration of the three crack nucleation defect sizes used to calibrate the critical distance method.

The results of this study will allow us to discuss the stability of the critical distance method depending on the considered crack nucleation length taking into account the microstructure effect.

2. Materials

The studied material is the C35 steel (AISI 1038 / AFNOR XC38) often used for rail applications. Its composition is in Table 1. This medium-carbon steel has two different components: ferrite and pearlite with a 50-50 ratio.

Table 1: C35 steel composition.

C	**Si**	**Mn**	**P**	**S**	**Cr**	**Mo**	**Ni**
0.32-0.39%	<0.40%	0.50-0.80%	<0.045%	<0.045%	<0.40%	<0.10%	<0.40%

To change the grain size d of this material, several heat treatments have been performed on cylindrical bars with an 18mm diameter. For most of the specimens, the heat treatment consists of a heating phase over the austenitic temperature (800°C) for a given time, then a cooling phase of the material. Two speeds of cooling have been used: The Air Cooling (AC) by getting the material out of the furnace at the end of the heating time, and the Furnace Cooling (FC) by shutting down the furnace and keeping the material inside. The FC is slower than the AC.

A specific heat treatment has been done to obtain a very small microstructure based on the method described by Shibata *et al.* [30]. It consists of a first austenitisation at 1100°C for 1h followed by Water Quenching (WQ). Then, two cycles of short austenitisation at 850°C for 10 minutes followed by WQ are performed. Finally, a last austenitisation at 850°C for 10 minutes is done, followed by AC. This method promotes grain germination instead of grain growth which results in a very thin microstructure.

Because heat treatments are performed in an air environment, there is a phenomenon of decarbonisation on the external part of the steel. To overcome this problem and have a homogeneous microstructure, 3mm have been removed from the surfaces of the bars after each heat treatment. Then, the specimens for monotonic traction, fatigue and fretting tests have been machined.

All the studied microstructures are presented in Figure 3. The mean grain size of ferrite and pearlite grains is measured using the linear intersection method (standard NF EN ISO 643/2624 [31]) after mirror polishing and chemical attack (Nital 5%) to reveal the microstructure. In the end, five ferrite-pearlite microstructures with grain sizes from 3µm to 29µm have been studied. Because our investigation needs to compare the fretting cracking response versus conventional fatigue parameters such as $\sigma_{d,-1}$, ΔK_0 and b_0, a dedicated characterisation of each microstructure have been undertaken.

d=3±1µm (HT: 850°C – 10 min / WQ cycles)	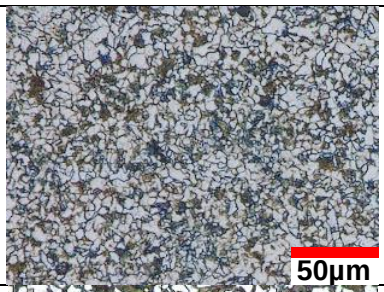
d=6±0.7µm (HT: AC 850°C – 1h)	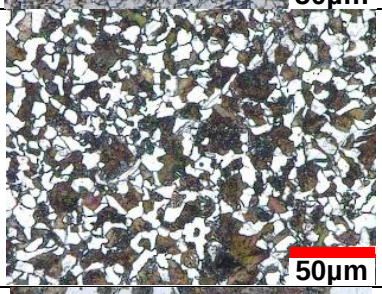
d=12±0.9µm (HT: FC 1000°C – 1h)	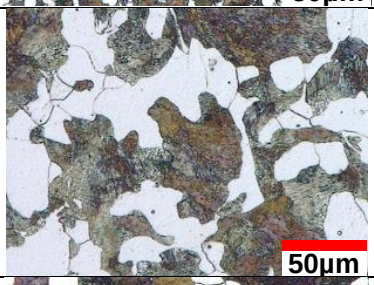
d=20±3µm (HT: FC 1000°C – 25h)	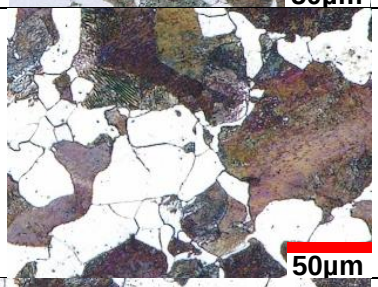
d=29±4.3µm (HT: FC 1100°C – 25h)	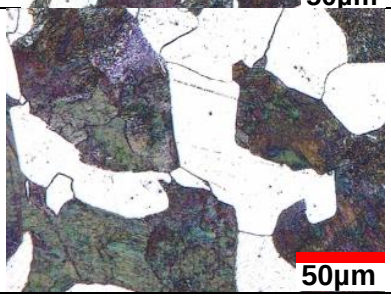

Figure 3: Microscope pictures and grain sizes of the C35 steel after heat treatments.

3. Monotonic traction and fatigue properties

3.1. Traction properties and hardness

Traction tests on dogbone-shaped specimens were performed to obtain the monotonic properties of three of the five microstructures (6, 12 and 29µm). Displacements were measured along the three space directions using digital image correlation thanks to speckles on the specimen and two cameras (as described in [32]). This method allowed us to obtain the

transverse parameters of the material such as the Poisson ratio. For each tested grain size, three monotonic traction tests were performed. There was good reproducibility.

The mean traction curve for each grain size is plotted in Figure 4 and gives the Young modulus E, the Poisson ratio ν, the yield strength σ_y and the ultimate tensile strength σ_u (cf. Table 2).

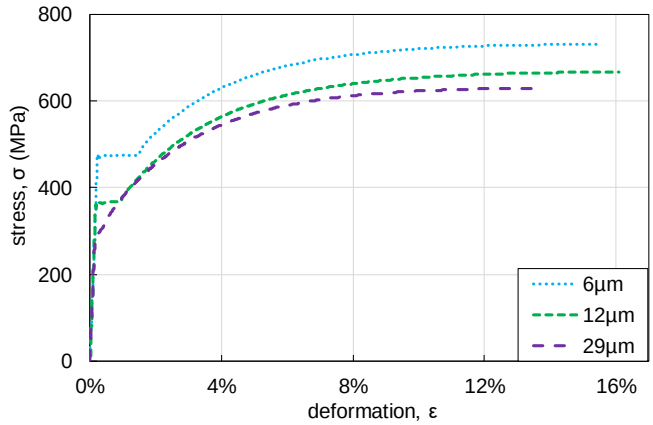

Figure 4: Traction curves for different grain sizes of the C35 steel.

Table 2: Traction properties and hardness for five C35 steel microstructures

d (µm)	3	6	12	20	29
σ_y (MPa)	/	480	360	/	280
σ_u (MPa)	/	720	670	/	620
E (GPa)	/	210	207	/	196
ν	/	0.29	0.29	/	0.32
HV	242	206	182	181	173

We observe an increase in the yield stress, ultimate stress and Young's modulus with decreasing grain size. To confirm this tendency, and as traction tests were not available for all microstructures, Vickers hardness tests (with a 3kg mass) were done in parallel. Five tests were performed for each microstructure and the mean values are given in Table 2. The hardness as a function of one over the square root of the grain size is plotted in Figure 5. The red dot corresponds to the value of the C35 steel used in Yameogo [33] and Kubiak's [34] research works. The comparison with latter literature data will allow us to confirm the various results obtained during the given investigation.

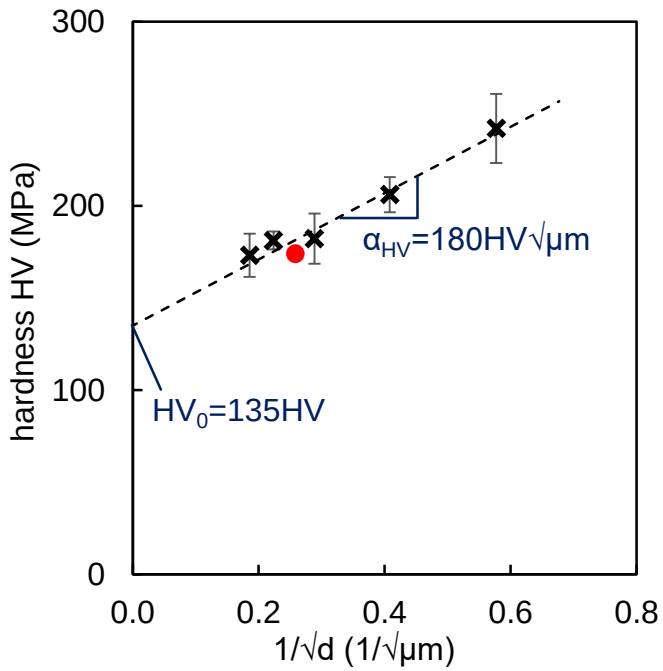

Figure 5: Hardness Vickers as a function of one over the square root of the grain size for the C35 steel (black crosses: experimental values from authors; red dot: from Yameogo and Kubiak's works)

It can be observed that the hardness HV follows a linear law:

$$HV = \alpha_{HV} \times \frac{1}{\sqrt{d}} + HV_0 \quad (1)$$

With α_{HV}=180MPa√µm and HV_0=135MPa.

This relation confirms the link between the hardness and the grain size presented in the Hall-Petch equation [35].

3.2. Fatigue properties

To use a multiaxial fatigue criterion and determine the critical distance, the traction-compression fatigue limit is needed for each microstructure. Fatigue tests using dogbone-shaped specimens were performed. The diameter of these specimens was 6 mm. For all the tests, the stress ratio is R=-1 ($R=\sigma_{min}/\sigma_{max}$), the frequency is f=40Hz and the maximal number of cycles is N_{max}=10,000,000.

More specifically, the Dixon staircase method [36,37] has been applied. In this method, a test is performed at a fixed stress. If it breaks before N_{max}, the next test is conducted with a lower stress. On the opposite, if it does not break within the 10,000,000 cycles, the next test is done with a higher stress. The stress difference between two steps is kept constant along the steps. In the end, this method gives the fatigue limit for each material and the standard deviation after at least ten tests. In this paper, the stress increment between two steps is 5 MPa.

The S-N curves of the four microstructures studied in fatigue are plotted in Figure 6 and the fatigue limits are reported in

Table 3.

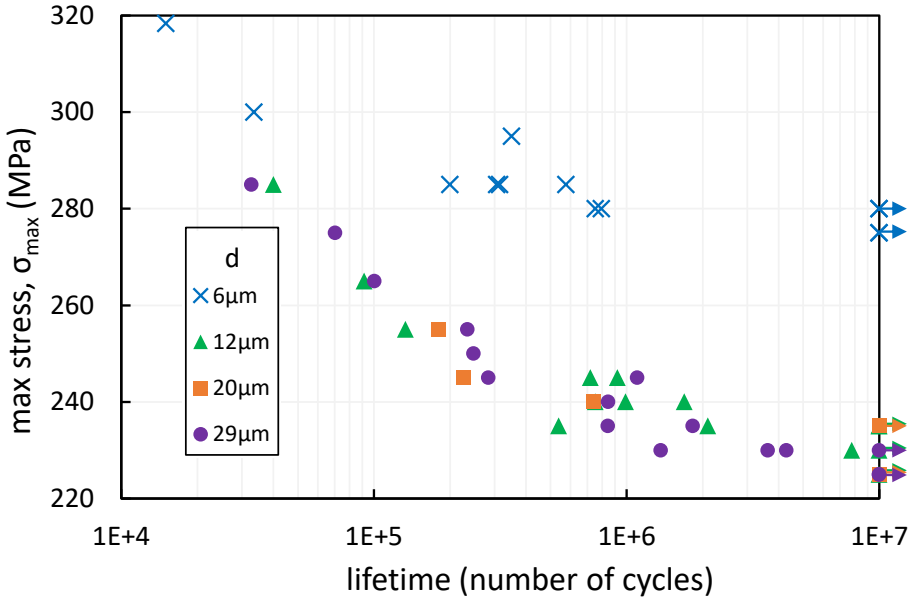

Figure 6: S-N curves (R=-1) for different microstructures of the C35 steel.

Table 3: Traction-compression fatigue limits (R=-1) for different grain sizes of the C35 steel (: extrapolated value from (2); $^{+}$: standard deviation from the staircase method but the norm is not verified)*

d (µm)	**3**	**6**	**12**	**20**	**29**
$\sigma_{d,-1}$ (MPa)	314*	$280\pm2^{+}$	239 ± 6	$237\pm2^{+}$	$229\pm2^{+}$

Fatigue strength increases with decreasing grain size, as reported in the literature [38,39]. From these results, we can plot the fatigue limit as a function of the inverse of the square root of the grain size (Figure 7). The red dot still corresponds to the reference from Yameogo and Kubiak's articles [33,34].

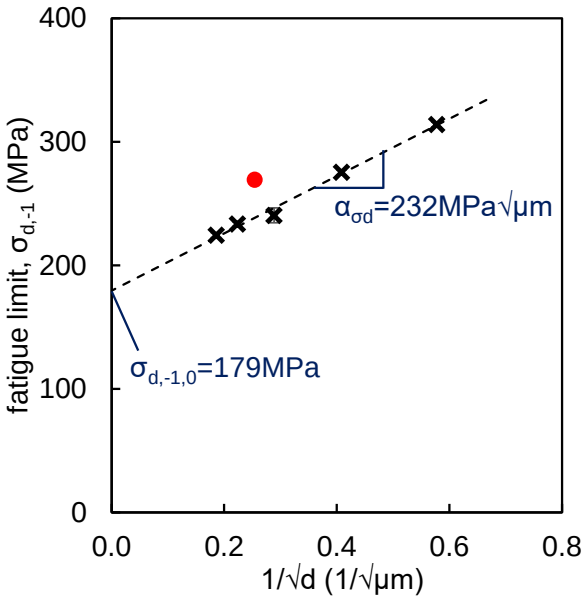

Figure 7: Traction-compression fatigue limit as a function of one over the square root of the grain size for the C35 steel (black crosses: experimental values from authors; red dot: from Yameogo and Kubiak's works)

It can be observed that the fatigue limit follows a linear law:

$$\sigma_{d,-1} = \alpha_{\sigma_d} \times \frac{1}{\sqrt{d}} + \sigma_{d,-1,0} \quad (2)$$

With α_{σ_d}=232MPa√µm and $\sigma_{d,-1,0}$=179MPa.

This relation confirms that the fatigue limit evolves as a function of the grain size with a similar dependency to the Hall-Petch equation. The point extracted from Yameogo and Kubiak's research works is slightly higher compared to the fitted curve. This difference may be explained by the fact that, in their works, the C35 steel was textured due to the applied manufacturing process leading to an anisotropy in the material which is not present in given specimens.

Finally, with these values, a correlation between the fatigue limit and hardness can be established for C35 steel (Figure 8).

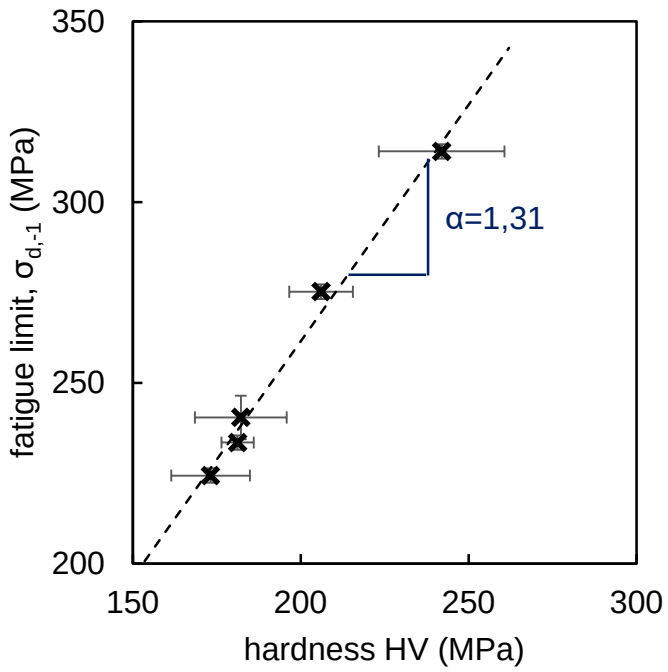

Figure 8: Traction-compression fatigue limit as a function of hardness Vickers for the C35 steel.

This curve shows a proportional relation between the fatigue limit and the hardness of the C35 steel:

$$\sigma_{d,-1} = \alpha \times HV \quad (3)$$

With α =1.31.

So, in this part, the monotonic and fatigue properties of the C35 steel were determined by taking into consideration the grain size.

4. Fretting cracking analysis

4.1. Methodology

4.1.1. Fretting experiment

In this paper, fretting tests were performed on a plane specimen made of the studied material (heat-treated C35 steel) against a cylinder made of 100Cr6 steel (AISI 52100) with a radius of 40mm. Both the plane and the cylinder samples were 8mm wide. The coefficient of friction between these two surfaces was equal to 0.8 and was obtained from Kubiak's research work [34]. The fretting setup is as described by Arnaud *et al.* [40].

All these tests were performed on an MTS hydraulic machine. Most of the parameters were constant: normal load P=4000N (Hertz contact pressure: p=668MPa; contact size: 2a=0.92mm), frequency f=15Hz and number of cycles N=1,000,000. The only parameter that changed between each test was the relative displacement amplitude δ* (and so the tangential load amplitude Q*).

4.1.2. Crack expertise

At the end of each fretting test, a fretting scar could be observed (Figure 9 at the top). To measure the crack length created by the fretting loading, the specimen was cut along the median axis. The cut surface was coated in epoxy resin and polished with SiC papers and felt disks with diamond solution (9µm and 3µm) and alumina (0.8µm). Projected crack length b could so be measured for each test. Projected crack length was chosen over real crack length as it is commonly used in the literature [27,41]. Several cut/polished planes were done to find the maximum length of the crack since this latter was not always observed along the median axis of the fretting scar.

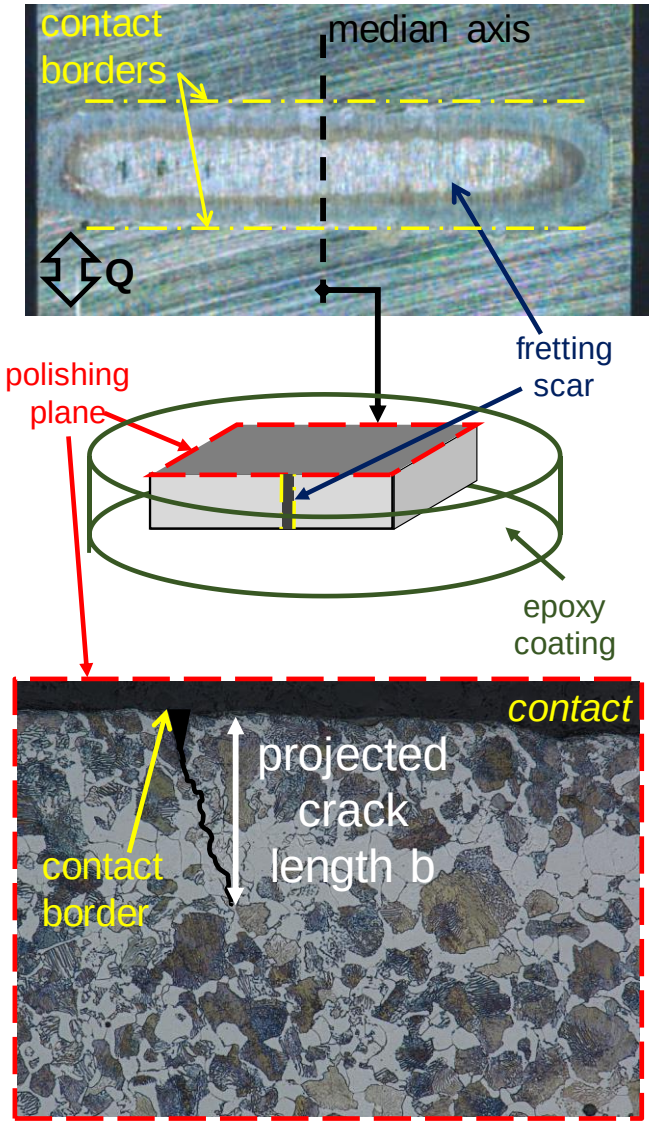

Figure 9: Post-fretting test crack measurement process.

Fretting cracks were systematically observed at the contact borders of the fretting scar with an inclination of around 30° toward the inner part of the cylinder/plane interface. It is interesting to note that, most of the time, the crack nucleated inside a ferrite grain (which is softer than pearlite). Moreover, the crack propagation was mostly transgranular.

4.1.3. FEM modelling

In parallel to the fretting tests, a 2D FEM model of the studied cylinder/plane contact was implemented using an ABAQUS/Standard code (Figure 10).

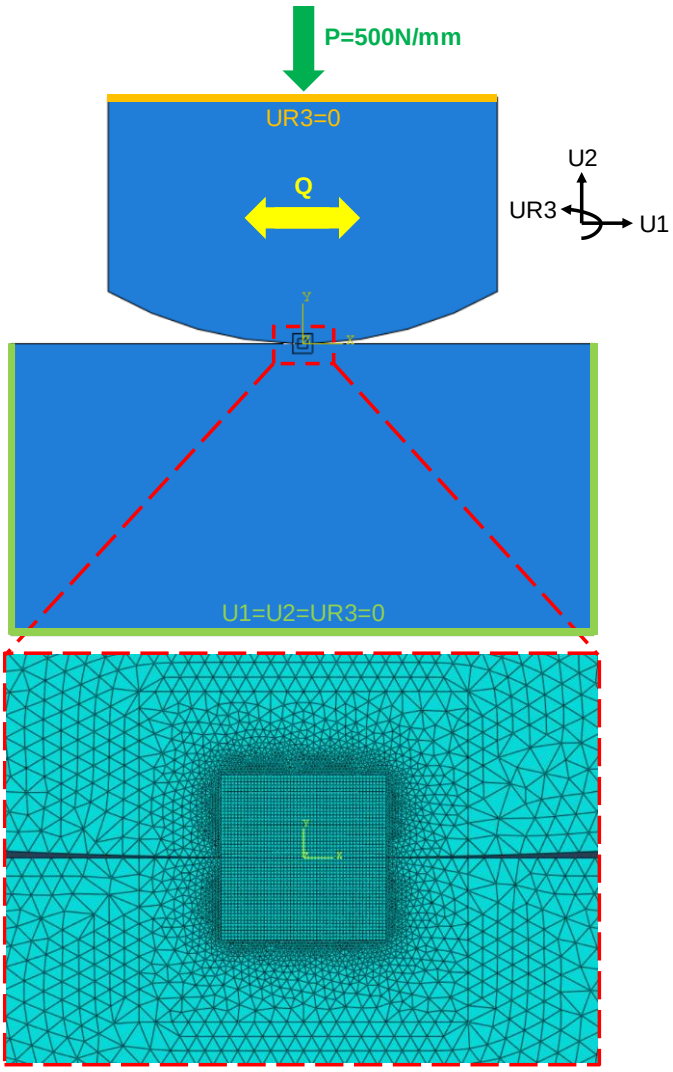

Figure 10: 2D cylinder/plane FEM model (top) and refined mesh under the contact (bottom).

The geometries and material were the same as in the fretting experiment (plane of C35 steel, cylinder of 100Cr6 steel with a 40mm radius). The contact was Lagrangian with a finite sliding formulation and a friction coefficient of 0.8. The mesh just under the contact (1mm large, 0.5mm deep) was composed of quadrilateral elements with a mesh size of 1µm. Outside this zone, the mesh elements were triangular and bigger as they were far from the contact. The plane was completely embedded (U1=U2=UR3=0) when the cylinder was only blocked in rotation (UR3=0). The normal load (P=500N/mm) and the cyclic tangential load Q, related to each experimental conditions, were applied. Unlike a gross slip condition, a partial slip contact, as applied in our study, must be controlled in tangential force amplitude and not in displacement. Indeed, the displacement measured on the fretting test involves not only the contact displacement but also the deformation of the total experimental assembly. On the

other hand, the measured tangential force does correspond to the tangential force applied to the contact. For all the simulations, the material behaviour was chosen to be linear elastic.

4.2. Results

4.2.1. Fretting crack length versus tangential load

For each microstructure, the projected crack length b can be plotted as a function of the tangential load amplitude Q*. All these curves are presented in Figure 11.

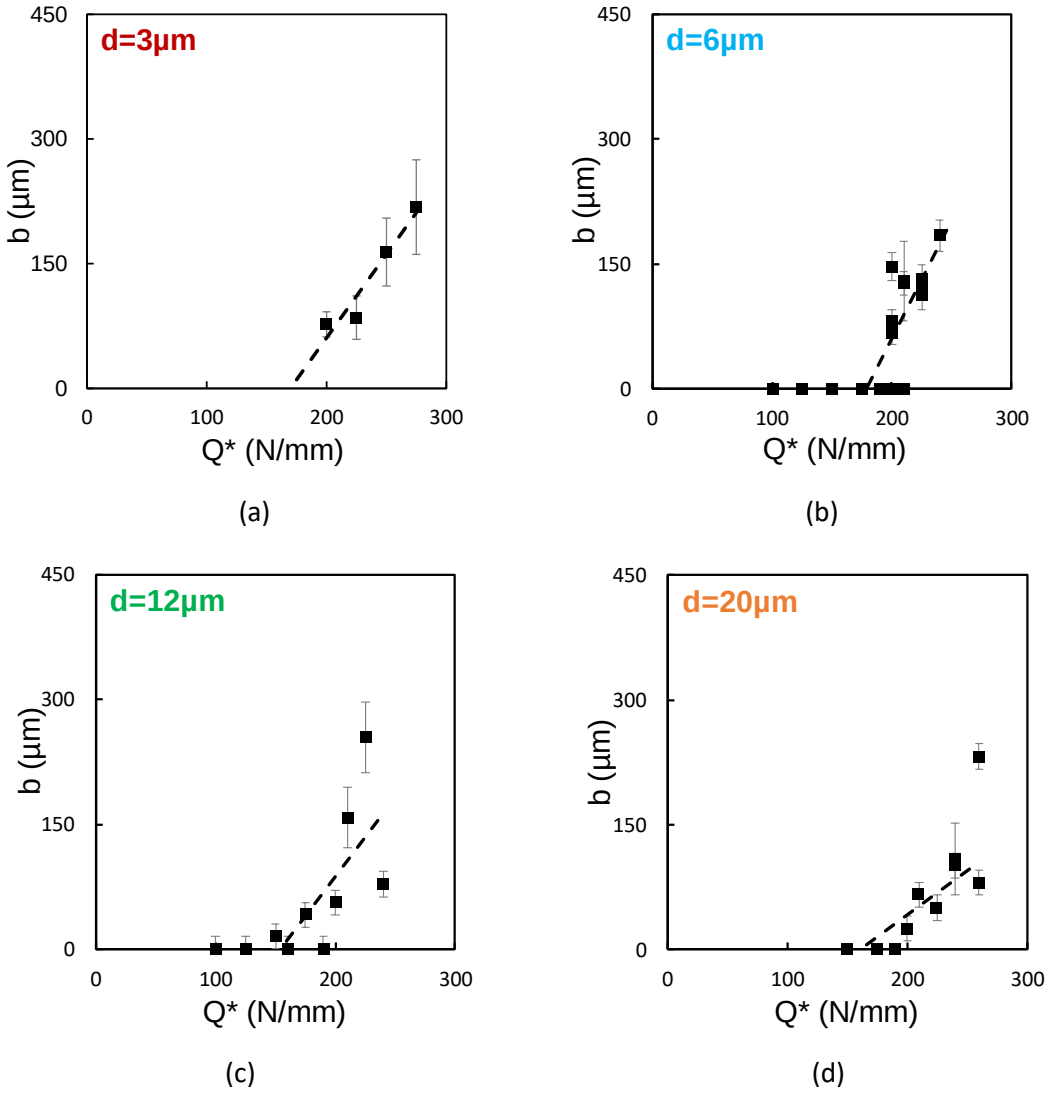

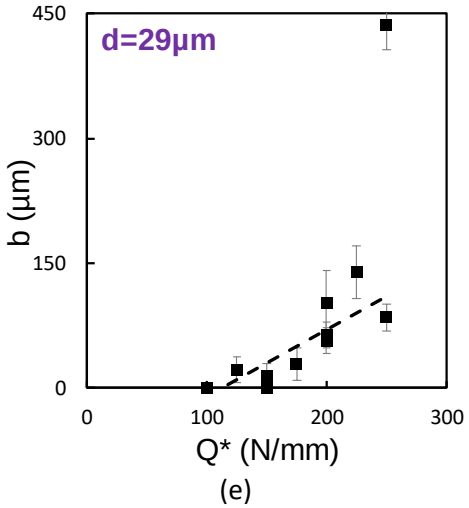

Figure 11: Projected crack length as a function of tangential load amplitude for different grain sizes of the C35 steel: : (a) d=3µm; (b) d=6µm; (c) d=12µm; (e) d= 20µm; (e) d=29µm (Q: tangential force amplitude; b: projected crack length).*

It can be observed that, for each grain size, the crack length follows a linear equation as a function of the tangential load amplitude:

$$b = \alpha_b (Q^* - Q_0^*) \quad (4)$$

With α_b the slope of the fitting curve and Q_0^* the point where it crosses the horizontal axis. The values of α_b and Q_0^* as a function of the grain size are reported in Table 4 and plotted in Figure 12.

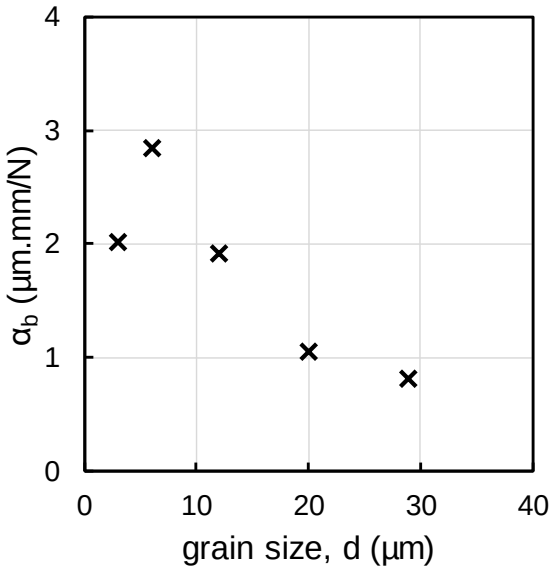

(a)

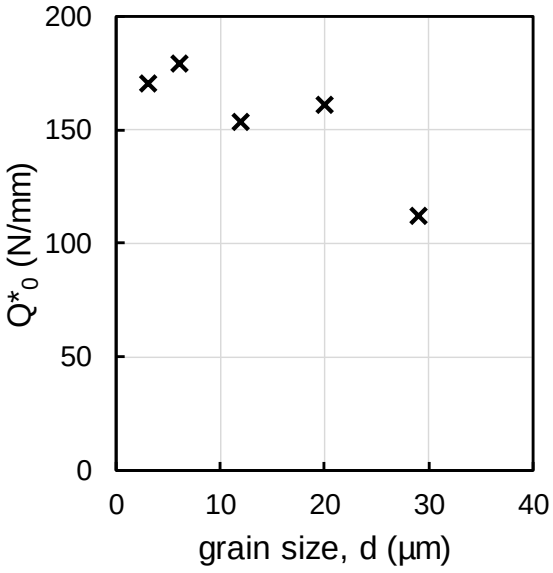

(b)

Figure 12: α_b (a) and Q^*_0 (b) values as a function of the grain size for the C35 steel.

Table 4: α_b and Q^*_0 values for different grain sizes of the C35 steel.

d (µm)	**3**	**6**	**12**	**20**	**29**
α_b (µm.mm/N)	2.01	2.84	1.91	1.05	0.80
Q^*_0 (N/mm)	170	179	154	161	112

The crack nucleation behaviour appears to be highly influenced by the grain size. It seems that the Q_0^* tends to decrease with the grain size which is consistent with the fatigue results where the bigger the grains the lower the fatigue limit. A similar dependency is also observed for α_b which leads to assuming that bigger grains slow crack propagation.

4.2.2. Identification of the crack threshold properties from the post-processing of fretting crack arrest

All these measured crack lengths correspond in fact to arrested crack situations. Indeed, partial slip fretting is characterised by the fact that after a sufficiently large number of cycles, the crack leaves the region influenced by the contact and can therefore no longer propagate. A preliminary study we did in the same configuration confirms that, after N=1,000,000 cycles, the crack does no longer propagate. The stress intensity factors (SIF) at their crack tips correspond to a crack arrest condition. Using the corresponding SIF, it is possible to plot the Kitagawa-Takahashi [17] diagram for each microstructure and get the long crack arrest condition ΔK_0 and the short/long crack transition b_0 also called the El Haddad [23,24] parameter. This method is based on the fretting inverse method previously detailed in [41,42].

To compute the SIF, we use the Z-cracks software. A straight crack is implemented inside a 3D Abaqus mesh (Figure 13). Inside the crack, the contact is considered Lagrangian with a finite sliding formulation and a coefficient of friction of 0.8. This value of the crack lips coefficient of friction was obviously equal to the value measured during the variable displacement method for the fretting contact. It can be considered representative since similar small displacement amplitudes are occurring within the crack interface.

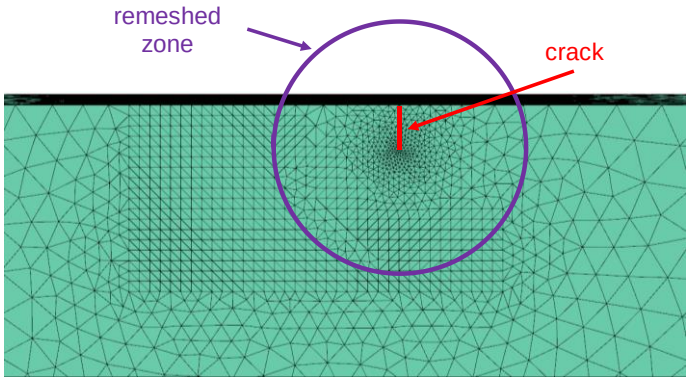

Figure 13: Abaqus 3D mesh with a crack inside.

Simulations were run and the mode I and mode II stress intensity factors of each crack were obtained at the tip of the crack. The integration method used in the Z-crack software is presented in [43]. As all the cracks were considered arrested, the crack arrest threshold of each crack is then defined using the following formula [44]:

$$\Delta K_{th} = \sqrt{{K_{I,max}}^2 + \left(K_{II,max} - K_{II,min}\right)^2} \quad (5)$$

Stress intensity factor threshold versus crack length graphs for each microstructure are plotted in Figure 14. On each graph, the stress intensity factor threshold related to long crack arrest condition ΔK_0 can be read as the asymptotic value of the fitted curve:

$$\Delta K_{th} = \Delta K_0 \sqrt{\frac{b}{b+b_{\Delta K}}} \quad (6)$$

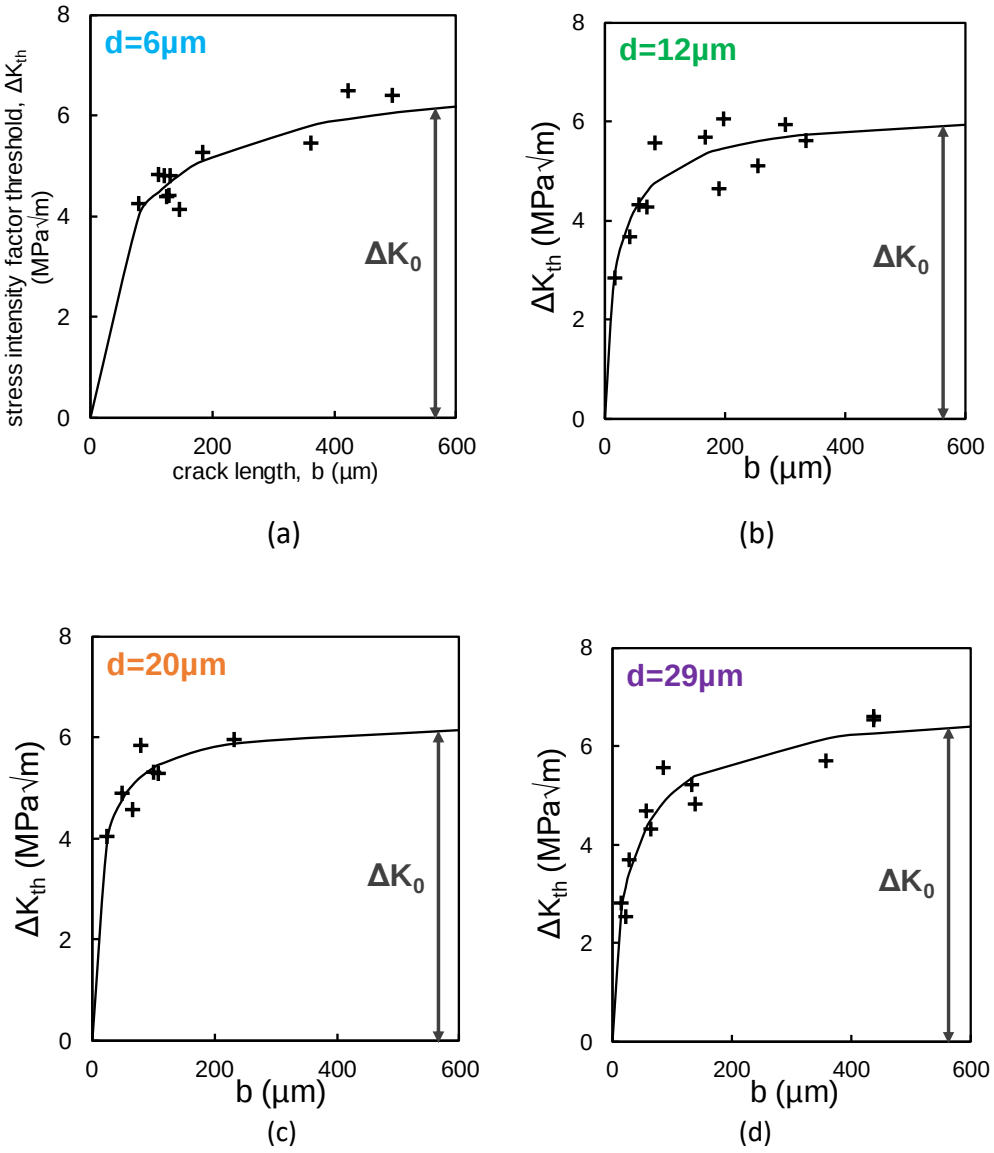

Figure 14: Kitagawa-Takahashi diagrams extracted from the fretting crack arrest analysis related to the different microstructures of the C35 steel investigated: (a) d=6µm; (b) d=12µm; (c) d=20µm; (e) d= 29µm.

Finally, with the value of ΔK_0, the El Haddad parameter can be calculated with:

$$b_0 = \frac{1}{\pi}\left(\frac{\Delta K_0}{Y.\sigma_{d,-1}}\right)^2 \quad (7)$$

With Y a geometric coefficient depending on the crack shape (Y=1.12 in the given contact geometry). All the ΔK_0 and the b_0 values are compiled in Table 5. Figure 15 displays the stress intensity factor threshold for long crack arrest condition ΔK_0 and the short/long crack transition b_0 as a function of the grain size. The red dot is still the reference from Yameogo and Kubiak's research works [33,34].

Table 5: Crack properties for different grain sizes of the C35 steel (: extrapolated values from (8) and (9))*

d (µm)	**3**	**6**	**12**	**20**	**29**
ΔK_0 (MPa√m)	6.69*	6.95	6.22	6.34	6.84
b_0 (µm)	153*	179	170	187	236

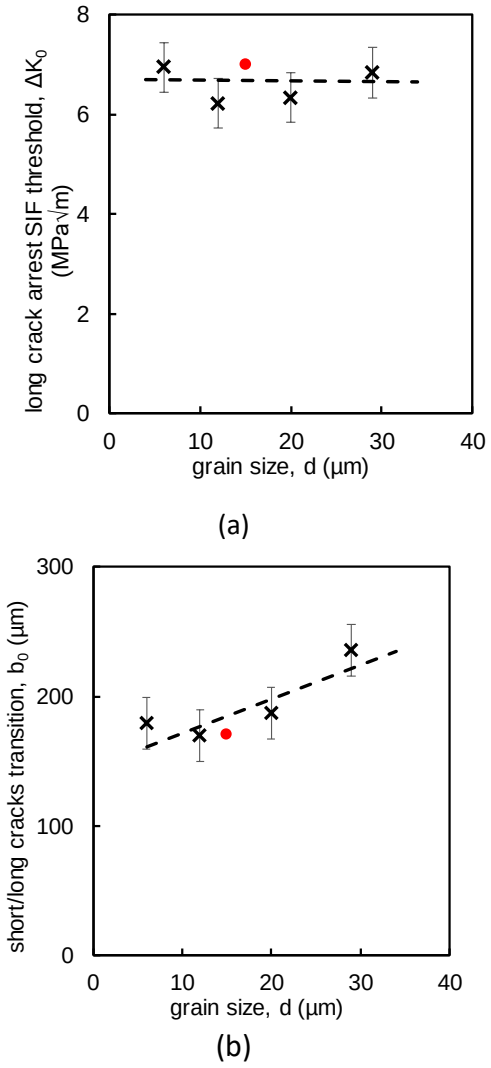

Figure 15: Stress intensity factor threshold for long crack arrest condition (a) and short/long crack transition (b) as a function of the grain size of the C35 steel (black crosses: experimental values from authors; red dot: from Yameogo and Kubiak's works)

It can be observed that ΔK_0 tends to remain constant whereas the short/long crack transition increases linearly with the grain size. The following equations can be written:

$$\Delta K_0 = 6.69 MPa\sqrt{m} \quad (8)$$

$$b_0 = \alpha_{b_0} \times d + b_{0,0} \quad (9)$$

With α_{b_0}=2.65 and $b_{0,0}$=145µm.

Unfortunately, it was not possible to complete sufficient fretting tests on the 3 µm microstructure to plot the complete Kitagawa-Takahashi diagram. Therefore, to estimate both

ΔK_0 and b_0 for such a microstructure, equations (8) and (9) were used to extrapolate these required values: ΔK_0 (3µm) = 6.69 MPa$\sqrt{m}$; b_0 (3µm) = 153 µm.

5. Stability of the critical distance method considering the defect size

5.1 Identification of crack nucleation thresholds

With the fretting and fatigue results from the previous parts, it is possible to calculate the critical distance for each microstructure. However, to do so, the tangential load amplitude threshold needs to be implemented into the numerical simulation. So the question is how to determine this threshold as it depends on the considered crack nucleation length. Indeed, the longer the crack length, the higher the tangential load threshold. As detailed in the introduction, three hypotheses are taken into account:

- 0µm: theoretical crack nucleation condition, it corresponds to the tangential load where the fitted curve crosses the horizontal axis,
- d (1 grain length): this condition assumes that the crack has initiated if it has crossed at least one grain of the material,
- b_0: the short/long crack transition which was described as a crack arrest boundary blocking in many aspects the extension until failure.

These three hypotheses are resumed in Figure 16 and all the thresholds are reported in **Erreur ! Source du renvoi introuvable.** for the five grain sizes d and the three considered crack nucleation lengths b_{CN}.

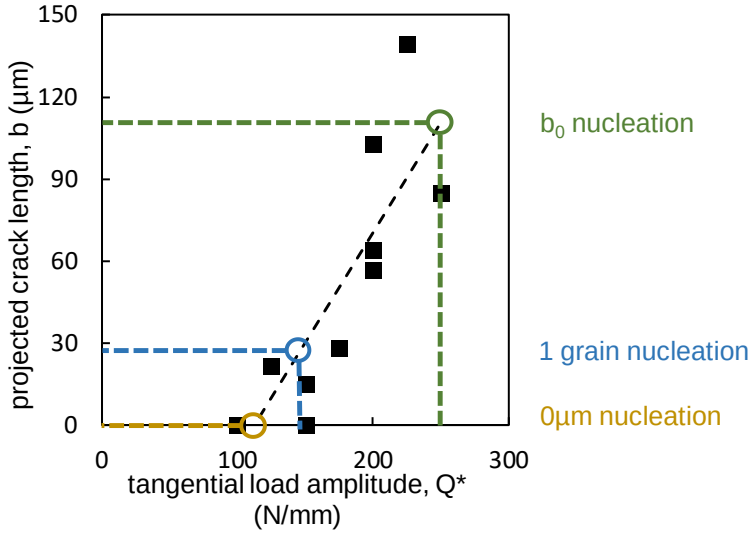

Figure 16: Crack nucleation length hypotheses.

Table 6: Crack nucleation tangential load amplitudes for different crack nucleation lengths and grain sizes of the C35 steel

	b_{CN} (µm)		
d (µm)	**0µm**	**d**	**b_0**
3	Q^*_{CN} (N/mm) = 170	171	246
6	179	181	242
12	154	160	243
20	161	180	334
29	112	149	395

5.2 Fretting Calibrated Critical Distance

To calculate the equivalent stress of the fatigue criterion, the tangential load threshold has to be injected as a loading condition in the numerical simulation. Then a multiaxial fatigue criterion is calculated on a normal line below the hotspot. The multiaxial fatigue criterion used in this study is the Smith-Watson-Topper criterion (SWT) [4].

The SWT criterion is based on a "critical plane" approach, which means that, for each point in the material (at least in the area we are interested in, just under the contact in this case), the crack nucleation risk is evaluated for several planes with different orientations. In the case of this specific criterion, the parameter calculated in each plane is Γ_{SWT} which is the product of the maximal stress in this plane $\sigma_{n,max}$ and the associated strain ε_a. The plane where this parameter is the highest is called the "critical plane" and is where the crack is supposed to appear first. Figure 17 (a) presents the field of Γ_{SWT} under the cylinder/plane contact. It is important to note that the critical plane can be different at each point. Finally, to obtain an equivalent stress, this parameter has to be linked with the Young modulus of the material with the following equation:

$$\sigma_{SWT} = \sqrt{\Gamma_{SWT} E} = \sqrt{\sigma_{n,max} \varepsilon_a E} \quad (10)$$

The SWT criterion is then the comparison between this equivalent stress and the traction-compression fatigue limit $\sigma_{d,-1}$. The criterion predicts crack nucleation if:

$$\sigma_{SWT} > \sigma_{d,-1} \quad (11)$$

As the critical distance is determined for the crack nucleation condition, the correlation must be done at the fatigue limit:

$$\sigma_{SWT} = \sigma_{d,-1} \quad (12)$$

So, to determine the critical distance, the SWT equivalent stress is plotted along the depth under the hotspot (Figure 17 (b)). It can be observed that there is only one point where equality (12) is satisfied, allowing the determination of the optimum critical distance.

(a)

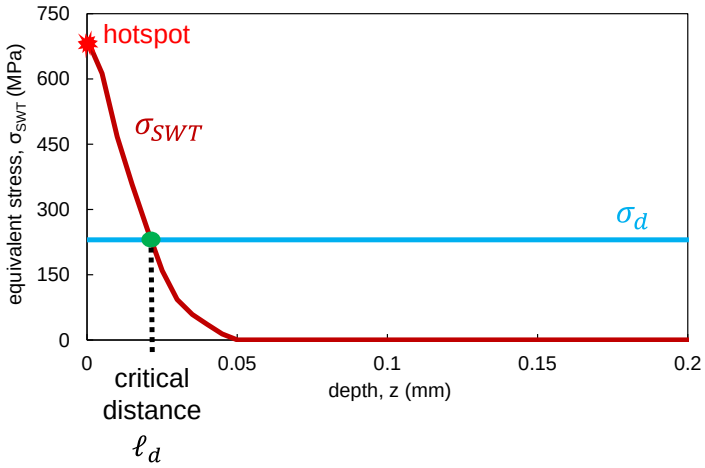

(b)

Figure 17: SWT parameter field under the contact (a); Critical distance determination under the hotspot (b).

This process is repeated for all five microstructures and all three nucleation hypotheses. The obtained critical distances are reported in Table 7 and plotted in Figure 18.

Table 7: Critical distances for different crack nucleation lengths and grain sizes of the C35 steel

	b_{CN} (µm)		
d (µm)	**0µm**	**d**	**b_0**
3	ℓ_d (µm) = 27	27	56
6	35	36	62
12	30	33	70
20	36	44	134
29	21	34	191

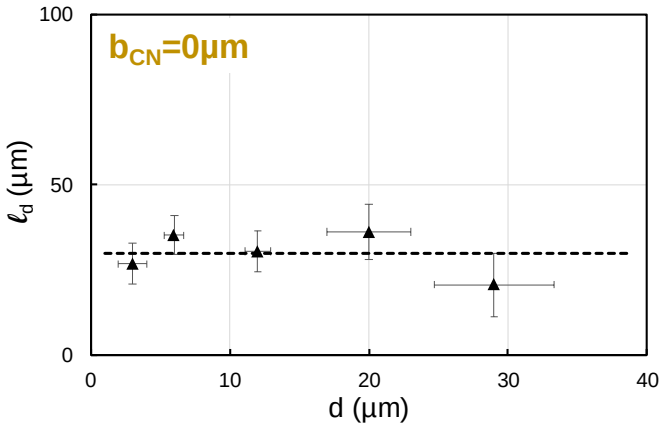

(a)

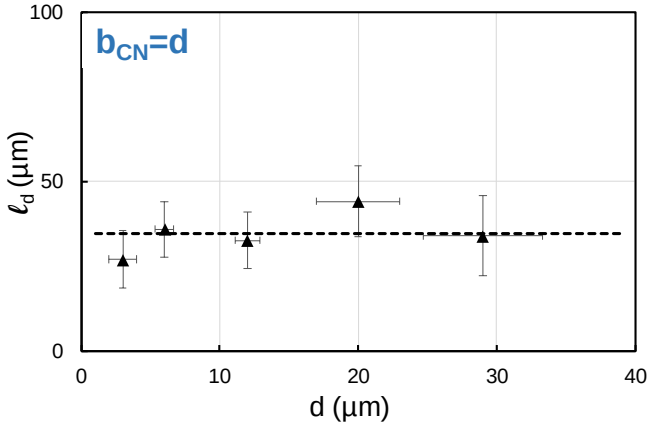

(b)

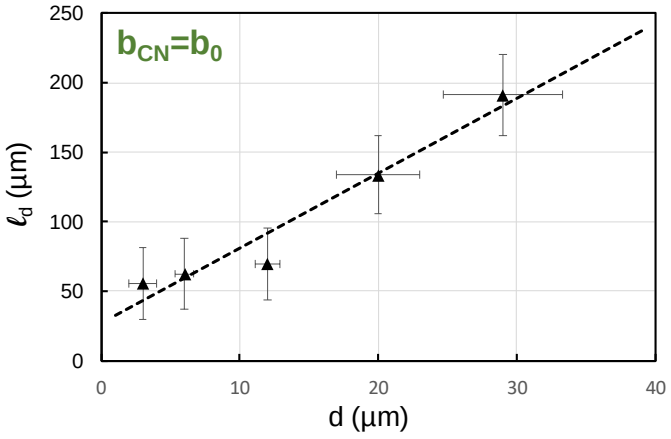

(c)

Figure 18: Critical distance established for the SWT criterion (ℓ_d) as a function of grain size (d) for different crack nucleation lengths (b_{CN}) (C35 steel).

It can be observed that for the first two hypotheses (b_{CN}= 0µm and b_{CN}= d), the critical distance remains stable although some scatter. On the opposite, the critical distance increases linearly with the grain size when b_{CN}= b_0.

For each nucleation hypothesis, a relation between critical distance and grain size can be written:

$$\ell_d(b_{CN} = 0\mu m) = 28\mu m \quad (13)$$

$$\ell_d(b_{CN} = d) = 33\mu m \quad (14)$$

$$\ell_d(b_{CN} = b_0) = \alpha_{\ell_d,b_0} \times d + \ell_{d,b_0,0} \quad (15)$$

With α_{ℓ_d,b_0}=5.15 and $\ell_{d,b_0,0}$=41µm.

For all the crack nucleation length hypotheses, the relative error E% of the fitted curve compared to the experimental values is calculated as follows and reported in Table 8.

$$E\% = mean\left(\frac{|\ell_{d,fit} - \ell_{d,exp}|}{\ell_{d,exp}}\right) \quad (16)$$

Table 8: Error E% for the different crack nucleation lengths of the C35 steel.

b_{CN}	**0µm**	**d**	**b_0**
E%	18%	12%	13%

It appears that the relative error is smaller for b_{CN}= d and b_{CN}= b_0.

6. Discussion

In this part, the crack nucleation length will be discussed in light of the critical distance stability over the grain size. It is interesting to note that there are two kinds of dependency of the critical distance as a function of the grain size depending on the considered crack nucleation length.

On one hand, in the case of a relatively small defect size (b_{CN}=0µm and b_{CN}=d), the critical distance appears to be constant for all the grain sizes of the C35 steel. This means that the critical distance method is stable with the microstructure for small crack nucleation lengths. In other words, in this case, the critical distance can be determined for one specific grain size and can be used for every other grain sizes. This statement tends to support the critical distance method used in many previous research works [11–13,15] where b_{CN} was related to the grain size.

Moreover, the b_{CN}=d hypothesis seems interesting from a physical point of view as a link can be made with fatigue where the grain is the scale of the first damage (persistent slip bands) [25–28]. Indeed, High Cycles Fatigue phenomenon can be associated with plasticity phenomena at the grain scale (elastic shakedown, plastic shakedown, ...). That is why a crack smaller than the grain size does not seem to be relevant to determine an equivalent stress. Besides, as detailed by [45], the grain boundary can be considered the first microstructural

barrier stopping the crack extension. So again b_{CN}= d is consistent with a crack arrest physical description of the fretting-fatigue process.

On the other hand, if a longer defect size is considered (b_{CN}= b_0), it can be observed that the critical distance is not constant anymore and linearly increases with the grain size. As the short/long crack transition also has such a link with the microstructure, it consolidates Taylor's approximation (ℓ_d= 0.5b_0) [16] which states a link between the critical distance and b_0.

To investigate this ℓ_d-b_0 dependency, Figure 19 plots the evolution of the ratio $\psi_{\ell_d} = \ell_d/b_0$ as a function of the grain size.

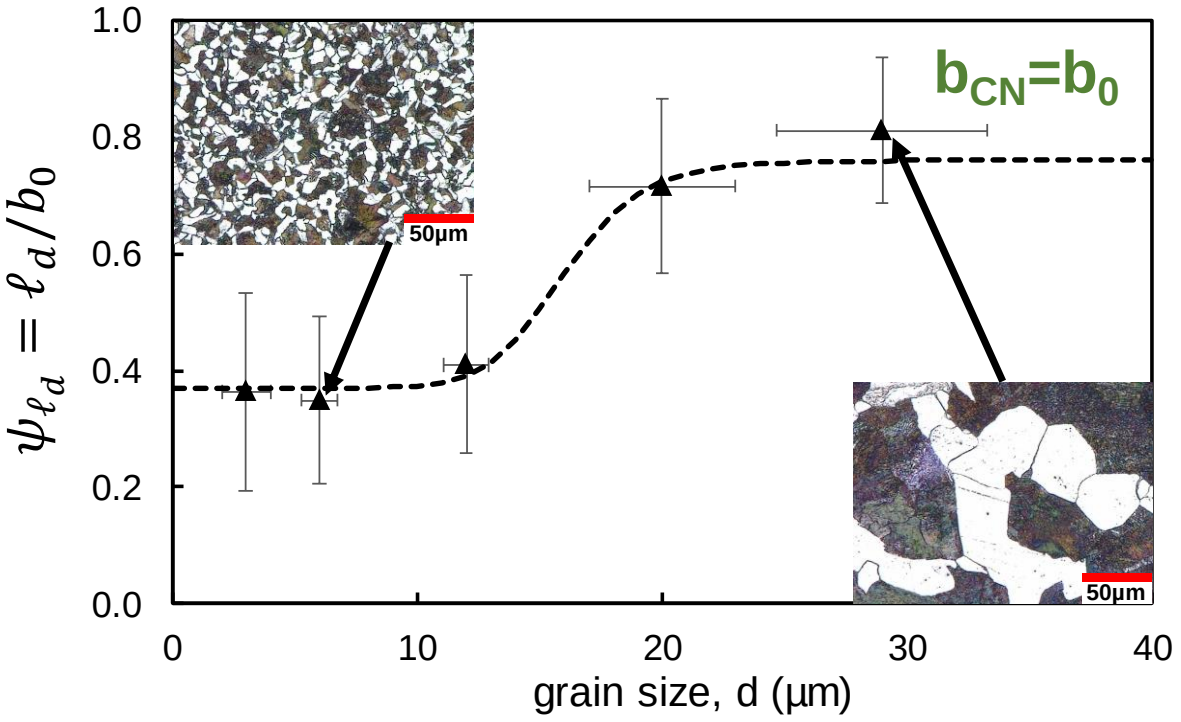

Figure 19: Critical distance over short/long crack transition as a function of the grain size considering a b_0 crack nucleation length (C35 steel)

A rising sigmoid evolution can be observed. For grain sizes smaller than 10µm, the ℓ_d /b_0 ratio displays a constant but low value around:

$$d < 10\mu m, \psi_{\ell_d} = \psi_{\ell_d,SG} = \frac{\ell_d}{b_0} = 0.37 \quad (17)$$

For longer grain sizes, above 10µm, the ℓ_d/b_0 stabilises at:

$$d > 10\mu m, \psi_{\ell_d} = \psi_{\ell_d,LG} = \frac{\ell_d}{b_0} = 0.76 \quad (18)$$

Hence, from the given investigation, two constants can be chosen for the $\psi_{\ell_d} = \ell_d/b_0$ ratio depending on the grain size d. It is interesting to note that Taylor's approximation,

$\psi_{\ell_d,Taylor}$=0.5, is between these two extreme values. To provide a continuous description of this two-plateau response, a sigmoid formulation is proposed so that:

$$\psi_{\ell_d} = \psi_{\ell_d,SG} + \frac{1}{1+\left(\frac{d_{th}}{d}\right)^{n_d}} \times \left(\psi_{\ell_d,LG} - \psi_{\ell_d,SG}\right) \quad (19)$$

With d_{th}=16µm and n_d=10.

However, the physical explanation of this "staircase" evolution still needs to be elucidated.

To conclude, it can be argued that, whatever the chosen b_{CN} length scale, the critical distance is stable if the following conditions are satisfied:

$$\begin{cases} if\ b_{CN} = 0\ \mu m\ or\ b_{CN} = d\ \rightarrow\ \ell_d = cst \\ if\ b_{CN} = b_0\ \rightarrow\ \ell_d = \psi_{\ell_d} \times b_0\ with\ \psi_{\ell_d} = \begin{cases} \psi_{\ell_d,SG}\ if\ d < d_{th} \\ \psi_{\ell_d,LG}\ if\ d > d_{th} \end{cases} \end{cases} \quad (20)$$

Finally, one limitation of this study is that all of the numerical simulations were performed using only the elastic parameters of the material. A previous study on a similar C35 steel [34] shows that there is plasticity induced by the fretting loading under the contact and it may have an influence over the critical distance and its relation with the grain size. Further investigations are currently performed to take the cyclic plasticity into account and obtain more relevant critical distance values. Besides, more fundamental researches need to be done to explain why for small grain size flow the critical distance is constant, and why for larger crack sizes the optimal critical distance displays two constant ratios versus b_0 depending on the grain size.

7. Conclusion

An experimental and numerical study has been performed to fully characterise the nucleation process coming from the fretting loadings. More specifically, the microstructure and the defect size effects have been highlighted.

First of all, different grain sizes of the same medium-carbon steel have been achieved thanks to several heating and cooling processes. Several tests have been done to obtain the mechanical and fatigue properties required by the numerical simulations and the multiaxial SWT fatigue stress investigation.

In parallel, cylinder/plane fretting tests have been performed to determine the crack nucleation threshold for all the microstructures. They were also useful to determine the short/long crack transition by applying post-processing of the obtained arrested crack conditions.

All these data lead to different crack nucleation lengths for the five microstructures. These lengths corresponded to tangential load amplitudes that have been implemented in a FEM simulation to determine the optimal critical distances.

Two typical evolutions have been observed on the crack defect size:

- For small crack nucleation lengths (b_{CN}=0µm and b_{CN}=d), the critical distance appears to be not influenced by the microstructure;
- For b_{CN}= b_0, Taylor's theory assuming a dependency between ℓ_d and b_0 is verified. However, the ℓ_d /b_0 ratio is constant but displays two different values depending on the grain size of the microstructure.

References

[1] Rajasekaran R, Nowell D. Fretting fatigue in dovetail blade roots: Experiment and analysis. Tribol Int 2006;39:1277–85. https://doi.org/10.1016/j.triboint.2006.02.044.

[2] Petiot C, Vincent L, Dang Van K, Maouche N, Foulquier J, Journet B. An analysis of fretting-fatigue failure combined with numerical calculations to predict crack nucleation. Wear 1995;181–183:101–11. https://doi.org/10.1016/0043-1648(94)07026-1.

[3] Crossland B. Effect of large hydrostatic pressures on the torsional fatigue strength of an alloy steel. Int. Conf. fatigue Met., vol. 6, 1956, p. 12.

[4] Smith, K.N., Topper, T.H., Watson P. A stress-strain function for the fatigue of metals (stress-strain function for metal fatigue including mean stress effect). J Mater 1970;5:767–78.

[5] Papadopoulos I V. a High-Cycle Fatigue Criterion Applied in Biaxial and Triaxial Out-of-Phase Stress Conditions. Fatigue Fract Eng Mater Struct 1995;18:79–91. https://doi.org/10.1111/j.1460-2695.1995.tb00143.x.

[6] Ferré R, Fouvry S, Berthel B, Ruiz-Sabariego JA. Stress gradient effect on the crack nucleation process of a Ti-6Al-4V titanium alloy under fretting loading: Comparison between non-local fatigue approaches. Int J Fatigue 2013;54:56–67. https://doi.org/10.1016/j.ijfatigue.2013.03.005.

[7] Proudhon H, Fouvry S, Yantio GR. Determination and prediction of the fretting crack initiation: introduction of the (P, Q, N) representation and definition of a variable process volume. Int J Fatigue 2006;28:707–13. https://doi.org/10.1016/j.ijfatigue.2005.09.005.

[8] Taylor D, O'Donnell M. Notch geometry effects in fatigue: A conservative design approach. Eng Fail Anal 1994;1:275–87. https://doi.org/10.1016/1350-6307(94)90003-5.

[9] Taylor D. The theory of critical distances. Eng Fract Mech 2008;75:1696–705. https://doi.org/10.1016/j.engfracmech.2007.04.007.

[10] Fouvry S, Kubiak K. Development of a fretting-fatigue mapping concept: The effect of material properties and surface treatments. Wear 2009;267:2186–99. https://doi.org/10.1016/j.wear.2009.09.012.

[11] Amargier R, Fouvry S, Chambon L, Schwob C, Poupon C. Stress gradient effect on crack initiation in fretting using a multiaxial fatigue framework. Int J Fatigue 2010;32:1904–12. https://doi.org/10.1016/j.ijfatigue.2010.06.004.

[12] McCarthy OJ, McGarry JP, Leen SB. A finite element study of microstructure-

sensitive plasticity and crack nucleation in fretting. Comput Mater Sci 2011;50:2439–58. https://doi.org/10.1016/j.commatsci.2011.03.026.

[13] Fouvry S, Gallien H, Berthel B. From uni- to multi-axial fretting-fatigue crack nucleation: Development of a stress-gradient-dependent critical distance approach. Int J Fatigue 2014;62:194–209. https://doi.org/10.1016/j.ijfatigue.2013.05.016.

[14] Gandiolle C, Fouvry S. Stability of critical distance approach to predict fretting fatigue cracking: A "ℓopt-bopt" concept. Int J Fatigue 2016;82:199–210. https://doi.org/10.1016/j.ijfatigue.2015.07.016.

[15] Said J. Etude expérimentale et modélisation de la durée de vie en fretting-fatigue des conducteurs aériens pour le transport d'énergie. Ecole Centrale de Lyon, 2020.

[16] Taylor D. Geometrical effects in fatigue: a unifying theoretical model. Int J Fatigue 1999;21:413–20. https://doi.org/10.1016/S0142-1123(99)00007-9.

[17] Kitagawa S, Takahashi H. Application of fracture mechanics to very small cracks or the cracks in early stage. Proc 2nd ICM 1976;2:627–31.

[18] Westergaard HM. Bearing Pressure and Cracks. J Appl Mech 1939;6:49–53.

[19] Castro FC, Araújo JA, Zouain N. On the application of multiaxial high-cycle fatigue criteria using the theory of critical distances. Eng Fract Mech 2009;76:512–24. https://doi.org/10.1016/j.engfracmech.2008.10.014.

[20] Hattori T, Bin Ab Wahab MA, Ishida T, Yamashita M. Fretting fatigue life estimations based on the critical distance stress theory. Procedia Eng 2011;10:3134–9. https://doi.org/10.1016/j.proeng.2011.04.519.

[21] Zabala A, Infante-García D, Giner E, Goel S, Endrino JL, Llavori I. On the use of the theory of critical distances with mesh control for fretting fatigue lifetime assessment. Tribol Int 2020;142:105985. https://doi.org/10.1016/j.triboint.2019.105985.

[22] Pinto AL, Talemi R, Araújo JA. Fretting fatigue total life assessment including wear and a varying critical distance. Int J Fatigue 2022;156:106589. https://doi.org/10.1016/j.ijfatigue.2021.106589.

[23] El Haddad MH, Topper TH, Smith KN. Prediction of non propagating cracks. Eng Fract Mech 1979;11:573–84. https://doi.org/10.1109/ICMETC.2015.7449566.

[24] El Haddad MH, Smith KN, Topper TH. Fatigue Crack Propagation of Short Cracks. J Eng Mater Technol 1979;101:42–6. https://doi.org/10.1016/b0-08-043152-6/00516-7.

[25] Deng R, Yu G, Li H. Effect of grain size on slow fatigue crack propagation and plastic deformation near crack tip. Theor Appl Fract Mech 1987;7:37–40. https://doi.org/10.1016/0167-8442(87)90057-7.

[26] Srinivas M, Malakondaiah G, Rao PR. Influence of polycrystal grain size on fracture toughness of and fatigue threshold in Armco iron. Eng Fract Mech 1987;28:561–76. https://doi.org/10.1016/0013-7944(87)90053-1.

[27] Tokaji K, Ogawa T, Ohya K. The effect of grain size on small fatigue crack growth in pure titanium. Int J Fatigue 1994;16:571–8. https://doi.org/10.1016/0142-1123(94)90483-9.

[28] Morrison DJ, Moosbrugger JC. Effects of grain size on cyclic plasticity and fatigue

crack initiation in nickel. Int J Fatigue 1997;19. https://doi.org/10.1016/s0142-1123(97)00034-0.

[29] Ashton PJ, Harte AM, Leen SB. Statistical grain size effects in fretting crack initiation. Tribol Int 2017;108:75–86. https://doi.org/10.1016/j.triboint.2016.09.022.

[30] Shibata A, Daido S, Terada D, Tsuji N. Microstructures of pearlite and martensite transformed from ultrafine-grained austenite fabricated through cyclic heat treatment in medium carbon steels. Mater Trans 2013;54:1570–4. https://doi.org/10.2320/matertrans.MH201312.

[31] Barralis J, Maeder G. Métallurgie : élaboration, structures-propriétés, normalisation. 2005.

[32] Flament C, Salvia M, Berthel B, Crosland G. Digital image correlation applied to thermal expansion of composites. ICCM Int Conf Compos Mater 2013:5235–43.

[33] Yameogo A, Carrado A, Marechal AM, Pommier S, Prioul C, Lodini A. Residual stress redistribution due to cyclic loading in a railway wheel/axle assembly. J Neutron Res 2004;12:63–8. https://doi.org/10.1080/10238160410001734478.

[34] Fouvry S, Nowell D, Kubiak K, Hills DA. Prediction of fretting crack propagation based on a short crack methodology. Eng Fract Mech 2008;75:1605–22. https://doi.org/10.1016/j.engfracmech.2007.06.011.

[35] Hall EO. Variation of Hardness of Metals with Grain Size 1954:948–9.

[36] Dixon WJ, Mood AM. A Method for Obtaining and Analyzing Sensitivity Data. J Am Stat Assoc 1948;43:109–26. https://doi.org/10.1080/01621459.1948.10483254.

[37] Wallin KRW. Statistical uncertainty in the fatigue threshold staircase test method. Int J Fatigue 2011;33:354–62. https://doi.org/10.1016/j.ijfatigue.2010.09.013.

[38] Alzubi F, Timko M, Li Y, Toal R, Tovalin K, Es-Said OS. Large versus small grain sizes on fatigue life of aluminum aircraft wheels. Defect Diffus Forum 2019;391:174–94. https://doi.org/10.4028/www.scientific.net/DDF.391.174.

[39] Rolim Lopes LC, Charlier J. Effect of grain size and intergranular stresses on the cyclic behaviour of a ferritic steel. Mater Sci Eng A 1993;169:67–77. https://doi.org/10.1016/0921-5093(93)90599-A.

[40] Arnaud P, Fouvry S, Garcin S. Wear rate impact on Ti-6Al-4V fretting crack risk: Experimental and numerical comparison between cylinder/plane and punch/plane contact geometries. Tribol Int 2017;108:32–47. https://doi.org/10.1016/j.triboint.2016.11.023.

[41] de Pannemaecker A, Fouvry S, Buffiere JY. Reverse identification of short-long crack threshold fatigue stress intensity factors from plain fretting crack arrest analysis. Eng Fract Mech 2015;134:267–85. https://doi.org/10.1016/j.engfracmech.2014.11.001.

[42] De Pannemaecker A, Fouvry S, Brochu M, Buffiere JY. Identification of the fatigue stress intensity factor threshold for different load ratios R: From fretting fatigue to C(T) fatigue experiments. Int J Fatigue 2016;82:211–25. https://doi.org/10.1016/j.ijfatigue.2015.07.015.

[43] Geniaut S, Massin P, Moes N. Evaluation of stress intensity factors with G-theta method and level sets in Code-Aster. 11th Int Conf Fract 2005, ICF11 2005;2:1043–8.

[44] Baietto MC, Pierres E, Gravouil A, Berthel B, Fouvry S, Trolle B. Fretting fatigue crack growth simulation based on a combined experimental and XFEM strategy. Int J Fatigue 2013;47:31–43. https://doi.org/10.1016/j.ijfatigue.2012.07.007.

[45] Miller KJ. Materials science perspective of metal fatigue resistance. Mater Sci Technol (United Kingdom) 1993;9:453–62. https://doi.org/10.1179/mst.1993.9.6.453.